Visible-Light Induced Photocatalytic Activity of Electrospun-TiO$_2$ in Arsenic(III) Oxidation

Gong Zhang,[†,§] Meng Sun,[†,§] Yang Liu,[‡] Xiufeng Lang,[∥] Limin Liu,[∥] Huijuan Liu,*[,†] Jiuhui Qu,[†] and Jinghong Li*[,‡]

[†]Key Laboratory of Drinking Water Science and Technology, Research Center for Eco-Environmental Sciences, Chinese Academy of Sciences, Beijing 100085, China

[‡]Department of Chemistry, Beijing Key Laboratory for Microanalytical Methods and Instrumentation, Tsinghua University, Beijing 100084, China

[§]University of Chinese Academy of Sciences, Beijing 100039, China

[∥]Beijing Computational Science Research Center, Beijing 100084, China

Ⓢ *Supporting Information*

ABSTRACT: In practical implementation of TiO$_2$ semiconductors, utilization of their outstanding properties is mainly hindered by poor material quality and high operational costs. In this contribution, the electrospinning method was employed to fabricate N-doped mixed-crystalline TiO$_2$ with exposed high-energy facets. The Ti oxide transformation process was thoroughly studied. During the mixed crystal structure formation process, the high-energy facets could be preserved due to the lower calcination temperature and the protective role of polyvinylpyrrolidone (PVP) in the electrospinning process. In addition, after calcination, the N doping, generated by the decomposition of PVP, extended the absorption spectrum of TiO$_2$ to the visible region. These TiO$_2$ fibers exhibited superior photooxidation of arsenite (III) to arsenate (V) in both the UV and visible light regions, mainly attributed to the exposure of

high-energy facets, robust separation of photoexcited charge carriers between the anatase/rutile phases, and narrow band gap induced by the in situ N doping. Combining both robustness and scalability, the TiO$_2$ fibers produced via this electrospinning process have the potential for a broad range of applications.

KEYWORDS: *electrospinning, TiO$_2$, visible light irradiation, mixed phases, nitrogen doping, arsenite oxidation*
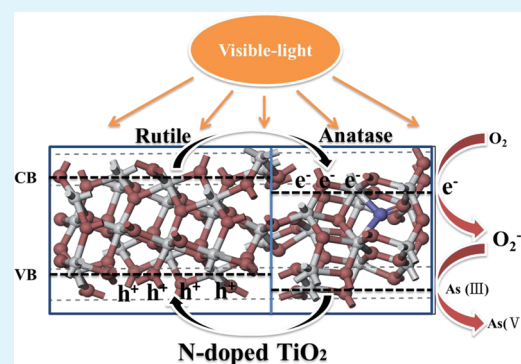
■ INTRODUCTION

Titanium dioxide (TiO$_2$) has been extensively used in many domains, particularly in the fields of catalysis, sensors, and electronic devices.[1−4] TiO$_2$ exists mainly in three polymorphs in nature, namely, anatase, rutile and brookite.[5,6] Anatase is an important form of TiO$_2$ that has a wider band gap (3.2 eV) than rutile (3.0 eV) but much stronger photocatalytic activity. Among the three main crystallographic forms of TiO$_2$, naturally metastable brookite is the least investigated in comparison with the comprehensively studied anatase and rutile phases because of the difficulties encountered in isolating it in pure form.[7] Furthermore, compared with any of single phase of TiO$_2$, many researchers believe that TiO$_2$ material composed of mixed phases exhibits much higher photoactivity.[8−10] What is more, the {001} facets, with a higher energy (0.90 J m^{-2}), are more conducive to higher reactivity, and they usually diminish rapidly during the crystal growth process.[11] Therefore, because of the transformation of anatase to rutile phase that occurs in the temperature range of 700−800 °C,[12,13] it seems impossible to control the exposure of higher-energy {001} facets in the phase transformation process. In addition, band-gap engineering is

crucial for optimizing the energy-harvesting capability of TiO$_2$ under solar radiation. Previous attempts to do so have involved adding traces of metal[14,15] and nonmetal impurities as dopants[16−18] to extend its activity into the visible-light region. However, these dopants tend to act as charge carrier recombination centers during the doping process.[19] Recently, interesting approaches based on in situ doping or dopant-free TiO$_2$ were proposed to overcome this limitation.[20,21]

Currently, arsenic pollution, both anthropogenic and natural, adversely affects the health of millions of people, especially in Southeast Asia, and various technologies have been utilized for its removal from drinking water.[22] Most absorbents exhibit much higher affinity for arsenate (As(V)) compared to arsenite (As(III)). In addition, As(III) is more toxic than As(V). Therefore, preoxidation of As(III) to As(V) is essential to develop the full potential of an arsenic removal system.[23−25] Photooxidation with TiO$_2$ as catalyst can be adopted as a
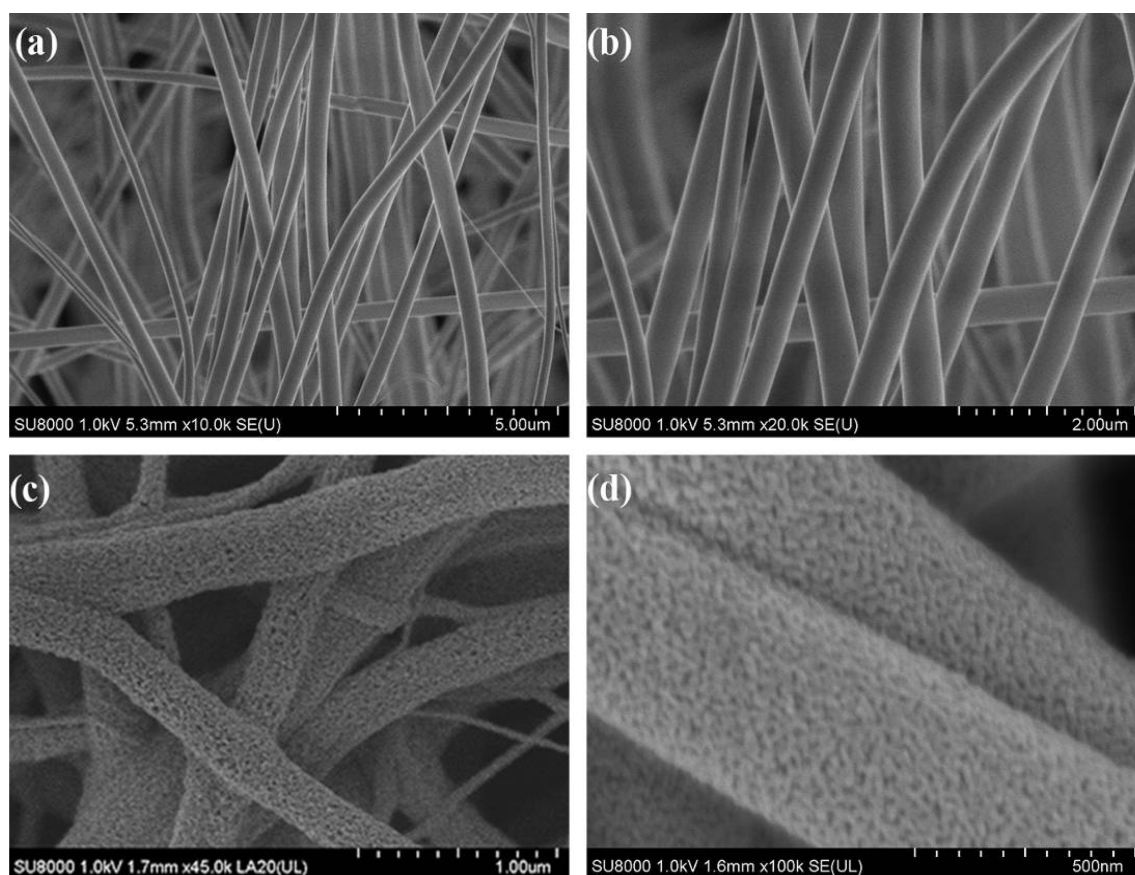
Figure 1. (a, b) SEM images of the as-spun fibers and (c, d) the TiO$_2$ fibers calcined in 500 °C.

measure to achieve this pivotal step. Although the oxidation of arsenic catalyzed by TiO$_2$ has been reported in recent literature,[26,27] poor quality and high operation costs restrain its practical application in environmental remediation.

Herein, to preserve the high-energy facets in the mixed-phase TiO$_2$ as much as possible, the electrospinning process was employed to fabricate TiO$_2$ fibers. Fibers were prepared via two steps: electrospinning synthesis followed by thermal treatment. The in situ nitrogen-doped TiO$_2$ fibers thus produced were applied for photooxidation of arsenic in the visible-light region.

■ EXPERIMENTAL SECTION

Materials. All chemical reagents were purchased and used without further purification, including Titanium(IV) butoxide (TBT) (98%, Fluka), polyvinylpyrrolidone (PVP) (M$_w$ = 1 300 000, Aldrich), nitric acid (HNO$_3$) (Guaranteed reagent, 65−68%), acetic acid (Guaranteed reagent, 100%), absolute ethanol (Guaranteed reagent, 100%), O$_2$ (99.99%), ammonium hydrogen phosphate, ammonium nitrate (Guaranteed reagent, Aldrich), and sodium metaarsenite (Analytical reagent).

Synthesis of N-Doped TiO$_2$ Fibers. Briefly, 2 mL of TBT and 900 mg of PVP powder were dissolved into a mixture containing 2 mL of acetic acid and 10 mL of absolute ethanol under vigorous stirring, to form a homogeneous polymer solution. Then the precursor solution was loaded into a syringe equipped with a blunt stainless steel needle, which was connected to a high voltage supply. The voltage for electrospinning was 15 kV, and the solution was fed at rate of 1 mL h^{-1} using a syringe pump. A stainless steel drum under the tip of the needle was used to collect the fibers. The as-spun product was dried in an oven at 80 °C overnight. Finally, the samples were heated in a quartz tube furnace at 500 °C for 180 min in oxygen at a ramp rate of 1 °C min^{-1}.

Fabrication of TiO$_2$ Powders. Correspondingly, two other species of TiO$_2$ powders were fabricated and denoted as E- and Sol-TiO$_2$. E-TiO$_2$ powders were obtained through calcining the electrospun precursor in oxygen at 500 °C. A sol−gel method was selected for fabricating the Sol-TiO$_2$ powders. Briefly, an absolute ethanol, water, and acetic acid mixture was added dropwise to a TBT solution to obtain Ti(OH)$_4$, and the follow-up thermal treatment was the same as above. To prepare N-doped P25 TiO$_2$ powders, pristine P25 TiO$_2$ powders (Degussa Company) were annealed under NH$_3$ flow at 500 °C for 3 h.

Material Characterization. The crystal structures of samples were characterized by powder X-ray diffraction (XRD) (X'Pert Pro PW 3040-Pro, PANalytical Inc.) using Cu Kα irradiation operating at 40 kV and 40 mA with a fixed slit. Raman spectra were measured on a Spectra-Physics model 127; the excitation source was He−Ne laser, and the resolution was 2 cm^{-1}. Specific surface area was measured by the volumetric method on an automatic adsorption instrument. The morphologies of TiO$_2$ fibers were observed with a Hitachi field-emission scanning electron microscope (FESEM). Lattices and fringes were obtained by JEOL high-resolution transmission electron microscopy (HRTEM). To investigate the light absorption and emission behavior of TiO$_2$, UV−visible absorption spectra were utilized under the diffuse reflection mode using an integrating sphere (UV2401/2, Shimadzu). XPS experiments were performed on the TiO$_2$ with a PHI5000 Versa Probe system (Physical Electronics, MN), and the samples were pressed to form a pellet prior to XPS measurement. The binding energy of XPS spectra was calibrated with reference to the C 1s peak at 284.8 eV.

Photoelectrochemical Measurements. The photocurrent action spectra were measured in a home-built two-electrode configuration experimental system, where TiO$_2$ powders coated on indium tin oxide (ITO)-coated glass by the doctor-blade method served as the working electrode, with an active area of 1 cm^2, and a platinum wire was used as the counter electrode in the electrolyte of 0.1 M KCl. A

512

dx.doi.org/10.1021/am506640k | ACS Appl. Mater. Interfaces 2015, 7, 511−518
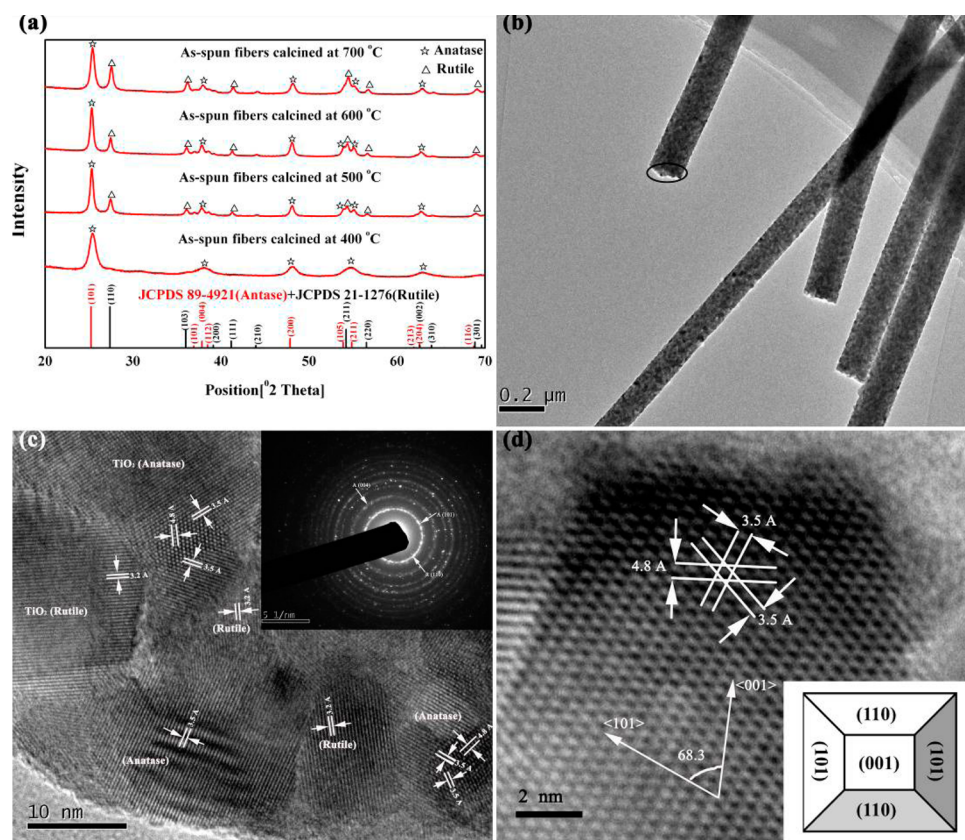
Figure 2. (a) XRD patterns of the TiO$_2$ fibers calcined at different temperatures. (b) TEM images showing the morphologies of the TiO$_2$ fibers calcined at 500 °C. (c) HRTEM image of the selected area and (inset) corresponding selected area electron diffraction result. (d) HRTEM image of the same area at a higher magnification, with inset showing a schematic drawing of a truncated tetragonal pyramid.

500 W Xe lamp with a monochromator was used as light source. The photoelectrochemical cell was illuminated from the ITO side of the TiO$_2$ electrode by the incident light. The photocurrent signal was collected using a lock-in amplifier (Stanford Instruments SR830 DSP). The monochromatic illuminating light intensity was 15 μW cm^{-2}. The illumination area of the working electrode was 0.12 cm^{-2}. All measurements were done after bubbling N$_2$ through the solution for 20 min and were controlled automatically by a computer. The chronoamperometry in this study was carried out using a Princeton Versa STAT 3 in a standard three-electrode cell, using Pt foil as the counter electrode and a Ag/AgCl electrode as the reference electrode. 0.1 M Na$_2$SO$_4$ purged with N$_2$ was used as electrolyte.

Testing of Photocatalyst. A commercial quartz reactor equipped with a 300 W xenon lamp was employed. Light with wavelength centered on 350 nm was employed for UVA irradiation, and wavelengths below 420 nm were cut off by an optical filter for visible-light irradiation. The photocatalytic activity was evaluated by oxidation of As (III) with initial concentration of 10 mg L^{-1}. A total of 50 mg of catalyst was added to 100 mL of As (III) containing solution. The original pH value was adjusted to 7.0 by a buffer solution. Before irradiation, to achieve adsorption equilibrium, suspensions were mixed under vigorous stirring in the dark for 30 min. After desired time intervals, samples were taken and centrifuged to separate the supernatant liquid from the catalysts. The two arsenic species were separated using Ultra Performance liquid chromatography with a PRP-X100 anion-exchange column (Hamilton Company) at 298 K.[28] The mobile phase, which was produced by dissolving 1.3602 g of (NH$_4$)$_2$HPO$_4$ and 0.8004 g of NH$_4$NO$_3$ into 1 L of water, and then adjusting the pH to 6.2, was delivered at 1.0 mL min^{-1} through the column. The follow-up mass spectrum (MS) detector was used to monitor the signal of the arsenic (m/z = 75) through the "time-resolved analysis" mode. To examine the roles of electrons and holes in the oxidation process, electron-spin resonance (ESR) spectra were employed for indirectly trapping the signals of generated reactive oxygen species (ROS) levels using 5,5-dimethyl-1-pyrroline N-oxide (DMPO) as scavenger. In addition, comparative experiments were performed by incorporating methanol, oxygen, and nitrogen gas into the photoreactor. Methanol acted as scavenger for photogenerated holes, oxygen can trap photogenerated electrons to generate superoxide anions, and nitrogen can deplete the oxygen content in the solution.

Computational Model and Details. To calculate the electronic structure of the N-doped anatase/rutile TiO$_2$ composite, we considered a thick anatase/rutile slab with 96 atoms (64 O atoms and 32 Ti atoms) for the composite. The structure of an N-doped anatase/rutile interface was modeled by adding one N atom to the anatase part of the anatase/rutile slab. The cell parameters and the atomic positions of the undoped and N-doped structures were optimized by performing the spin-polarized Perdew–Burke–Ernzerhof (PBE) exchange correlation functional within the generalized gradient approximation (GGA).[29] Considering that the PBE functional usually underestimates the band gap of semiconductors, cell parameters and atomic positions of the structure were also optimized by PBE+U calculations,[30] where a U(Tid) value of 4.2 eV was applied to Ti d states. The projector augmented-wave method (PAW) was employed to treat valence-core interactions with cores of [Ar] for Ti and [He] for O and C.[31] The plane wave cutoff energy of 400 eV and the Monkhorst–Pack grid with k-point mesh for integration in the Brillouin zone were used. The convergence threshold for self-consistent-field iteration was set at 10^{-5} eV, and all of the atomic positions were fully optimized until all components of the residual forces were smaller than 0.02 eV Å^{-1}. All of the calculations were carried out using the Vienna ab initio simulation package.[32]
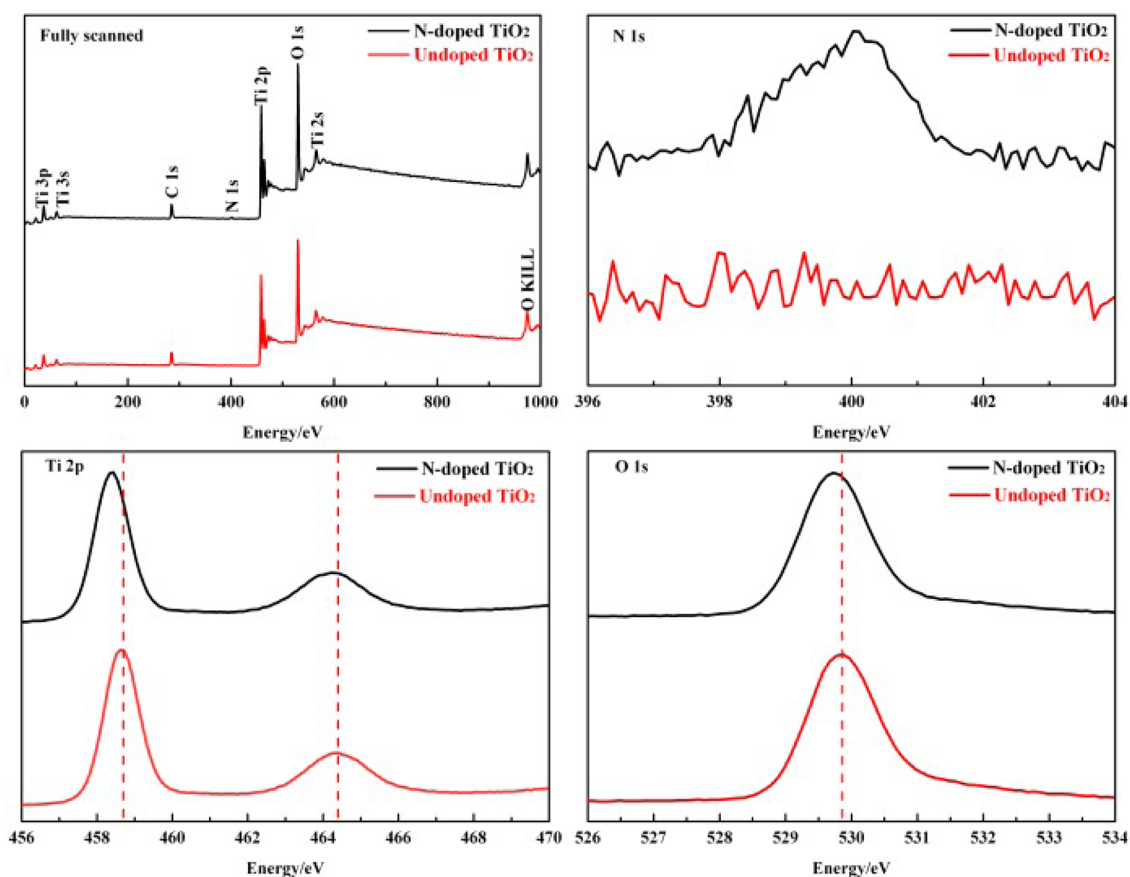
Figure 3. X-ray photoelectron spectra of fully scanned, N 1s, Ti 2p, and O 1s of the N-doped TiO$_2$ fibers and undoped TiO$_2$ powders (sol−gel).

■ RESULTS AND DISCUSSION

Morphology and Crystal Structure of the TiO$_2$. As shown in Figure 1a,b, fibers from 200 to 400 nm width and up to tens of centimeters long were sprayed onto the steel drum. These as-spun fibers possess a large surface area-to-volume ratio, which enables moisture to diffuse into the interior of fibers effectively, thereby ensuring complete hydrolysis of tetrabutyl titanate (TBT) to titanium hydroxide. As a result, titanium hydroxide uniformly coated by PVP was ordered along the direction of applied electric field. Furthermore, due to the rapid evaporation and decomposition of PVP molecules during the calcination process, PVP decomposition products act as a porogen to form uniform pores with average diameter of 7.5 nm, providing a large external surface that can be accessed readily by reactant molecules (Supporting Information, Figure S1).

X-ray powder diffraction (XRD) patterns of TiO$_2$ fibers calcined at different temperatures are shown in Figure 2a. Anatase crystals together with tiny rutile crystals were obtained in the 400 °C calcining condition. The crystals were further converted to a stable mixed-crystal phase as temperature was raised to 500 °C. Raman results indicated that the rutile content in the fibers was 23% (Supporting Information, Figure S2).[33] In addition, the resulting mixed-crystal phase showed high phase stability, retaining the structure even after being calcined at 600 °C. It is speculated that owing to the compact wrapping by PVP, the in situ hydrolysis of titanium hydroxide took place in an orderly manner, resulting in a shorter intermolecular distance compared to the traditional synthetic approaches. The novel molecular arrangement enhanced the thermal conductivity of titanium hydroxide, promoting the efficacy of the calcining process. In addition, because of the formation of nuclei occurring preferentially at surfaces, nucleation of rutile is influenced by the surface structure of titanium hydroxide.[34] When the high-voltage electric field was applied, the surface structure of titanium hydroxide was altered such that the surface energy was increased. As a result, nucleation of rutile occurred more readily due to the reduced free-energy barrier,[35] thereby enabling the rutile crystal phase to take shape at a relatively lower calcining temperature. To verify these theoretical predictions, two TiO$_2$ species were fabricated through conventional measures. As expected, in the equivalent calcining condition at 500 °C, only pure anatase crystal phase was obtained (Supporting Information, Figure S3).

Aiming to determine the specific phase structure, TEM analysis of TiO$_2$ crystals with crystalline lattice fringes was carried out as supplementary evidence (Figure 2b−d). Selected area electron diffraction patterns confirmed that the TiO$_2$ fibers showed mixed-crystal characteristics. The fringe spacing of 3.5 Å corresponds to the planes of {101} of the anatase, while spacing of 4.8 Å corresponds to {002} planes, indicating the top-bottom surfaces exposed by truncation are bounded by {001} facets.[11] The {001} facets, dominated by unsaturated atoms, tend to bond strongly with external species, which is therefore critical to high-efficiency photocatalytic reaction.[36] Unfortunately, surfaces with high reactivity usually diminish rapidly during the crystal growth process as a result of the minimization of surface energy. However, in the synthesis method used, PVP molecules might act as surfactant and shape controlling agent. Because of its polar character under an
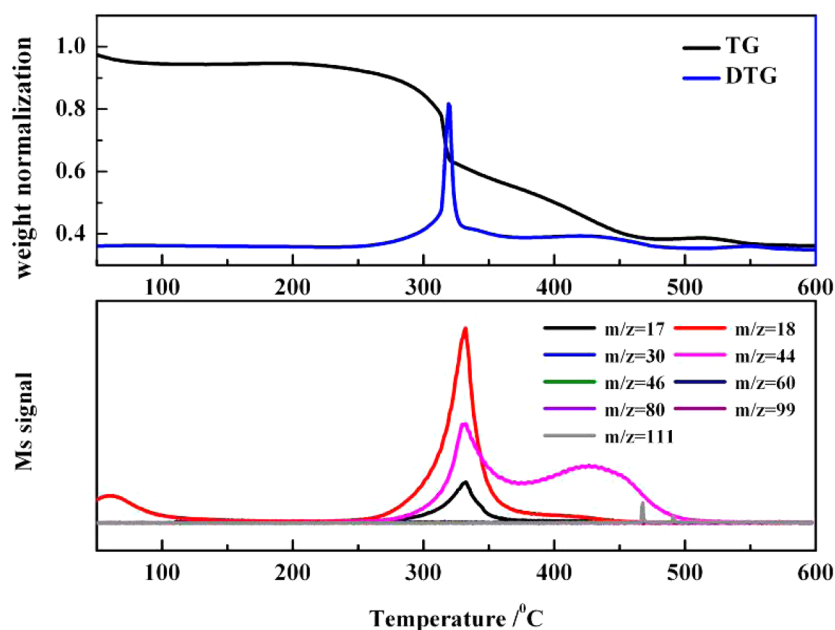
Figure 4. TG-differential thermal analysis curves of the as-spun fibers and TPO-MS profiles of selected gaseous products during the heating up process.

electric field, PVP preferentially bonded onto {101} facets of positively charged TiO_2 surfaces in acidic solutions. The firm binding could have hindered the growth of {101} facets and indirectly promoted the growth of {001} facets. In addition, as mentioned above, the required calcining temperature for the nucleation of rutile was greatly reduced after activation in the strong electric field, and this situation benefited the retention of high-energy facets. Hence, because of the presence of PVP and the low calcination temperature, the high-energy {001} facets can be preserved in the anatase/rutile mixed phase via the electrospinning process.

Nitrogen Doping Process of the TiO_2. The XPS measurements were performed to determine the composition of the N-doped TiO_2 fibers (Figure 3). A peak at 399.6 eV could be observed in the N 1s XPS spectrum, which was ascribed to Ti−N−O oxynitride. No band characteristic of N−H was found in Fourier transformed infrared spectra (FTIR) (Supporting Information, Figure S4), excluding the possibility that the peak at 399.6 eV was derived from N−H. Furthermore, the XPS analysis determined that the nitrogen content was 1.08 atom % for our TiO_2 fibers. In addition, the XPS spectrum also showed that the Ti 2p core of the undoped TiO_2 powders exhibited a Ti $2p_{3/2}$ peak at 458.8 eV and an O 1s peak at 529.9 eV. Peaks of Ti $2p_{3/2}$ in N-doped TiO_2 fibers occurred at 458.4 eV. Also, the O 1s peak shifted to 529.7 eV compared to the corresponding TiO_2 powders.

Theoretical calculations were performed to illustrate the N-doping of TiO_2 fibers. We constructed a rutile slab accompanied by an anatase slab to simulate the crystalline structure of the TiO_2 fibers. According to the results of the calculations, among possible combinations of rutile and anatase atomic surfaces, rutile {101} and anatase {001} established the closest arrangements. Furthermore, partial density of states (PDOS) analysis showed that both localized states are formed by the hybridization of 2p orbitals of N, 2p orbitals of O and 3d orbitals of Ti, which is consistent with the presence of Ti−N−O oxynitride in the N-doped interface (Supporting Information, Figure S5). Therefore, we speculated that, owing to the

particular configuration of PVP and $Ti(OH)_4$ molecules under the applied electric field, intermediates produced in situ could readily infiltrate and embed firmly in the lattice of anatase {001}. Eventually a small portion of N remained in the lattice of the anatase phase as interstitial doping atoms.

To gain a deep insight into the products involved during the Ti oxide transformation process, thermogravimetric (TG) analysis and temperature-programmed oxidation analysis (TPO) coupled with mass spectrometry (MS) were performed. As shown in Figure 4, the TG plot shows two major weight-loss regions. The first (up to about 100 °C) was attributed to desorption of water molecules absorbed by PVP molecules, which was further confirmed by MS analysis (m/z = 18). The second loss, starting at 200 °C, corresponded to the decomposition of PVP and dehydration of $Ti(OH)_4$ with evolution of H_2O (m/z = 18), CO_2 (m/z = 44), and NH_3 (m/z = 17). In addition, N-vinyl-2-pyrrolidone (m/z = 111), the monomer of PVP, which was derived from the pyrolysis of PVP molecules, could also be detected. Thus, the organic intermediates derived from PVP must be the N source contributing to the N-doping process.

Evaluation of the Photocatalytic Activity. For P25 TiO_2 powders, the absorption spectrum was cut off at ∼390 nm. However, for the N-doped TiO_2 fibers, a special add-on shoulder was imposed onto the cutoff edge of the absorption spectrum, extending the absorption from 390 to 450 nm (Figure 5). Extension of light absorption from UV to the visible range arose from the interstitial nitrogen atoms in the lattice. These nitrogen atoms induced N 2p levels near the valence band of TiO_2. In this way, the energy gap between the valence and the conduction bands of TiO_2 was reduced.

As observed in Figure 6a, under visible light irradiation, the oxidation process of arsenic(III) to arsenate(V) catalyzed by N-doped TiO_2 fibers (A/R = 3, calcined at 500 °C) was completed within 90 min. In addition, the photoactivity of two other TiO_2 fiber samples calcined at 400 and 700 °C and N-doped P25 TiO_2 powders were tested, respectively. Pure anatase phase was obtained via calcination at 400 °C. Under
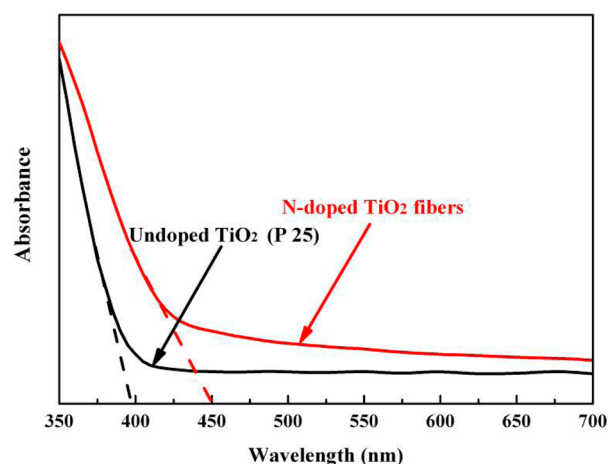
Figure 5. Diffuse reflectance spectra (DRS) of P25 TiO$_2$ powders and N-doped TiO$_2$ fibers.

700 °C treatment conditions, a mixed phase of anatase and rutile with a ratio of 1.8:1 was obtained. As shown in Figure 6b, when TiO$_2$ fibers calcined at 700 °C were used as catalyst, approximately 80% of As(III) was oxidized to As(V) within 90 min. In contrast, only 35% and 70% of As(V) was formed for the pure anatase and N-doped P25 TiO$_2$ photocatalytic systems, respectively, under the same experimental conditions. In addition, TiO$_2$ fibers calcined at 500 °C exhibited a similar

level of activity compared to the P25 TiO$_2$ powders under UV irradiation (Supporting Information, Figure S6).

The photocatalytic activity was mainly determined by the lifetime of the photoexcited charges. According to the photocurrent action spectra (Figure 7a), compared to pure-phase crystal, much higher photocurrent intensity was obtained in the mixed-phase crystal systems. This could be attributed to the transfer of photogenerated electrons from rutile to anatase lattice, which preserved the photogenerated charges that would have been lost to recombination. Moreover, the spectrum of N-doped TiO$_2$ fibers clearly shifted toward the visible range, which was further confirmed by chronoamperometry (Figure 7b). Besides, on account of their exposed high-energy facets, the TiO$_2$ fibers exhibited more affinity to the inorganic arsenic, also factoring in the catalytic performance.[10,37] Furthermore, in the UV range, the TiO$_2$ fiber electrode generated a similar photocurrent intensity to that of the P25 TiO$_2$ electrode, and a higher intensity compared to the N-doped P25 TiO$_2$ powder electrode. This could be attributed the reduced introduction of recombination centers in our N-doping process.[38−41]

To examine the roles of electrons and holes in the arsenic oxidation process, ROS generation on the surface of the TiO$_2$ fibers is possible due to the phenomenon of surface plasmon resonance (SPR). The generated electrons interact with O$_2$ adsorbed on the surface of the catalyst to form superoxide anions (O$_2^{\bullet-}$), while holes associate with hydroxyl ions (OH$^-$) to form hydroxyl radicals (●OH). Six characteristic peaks of the
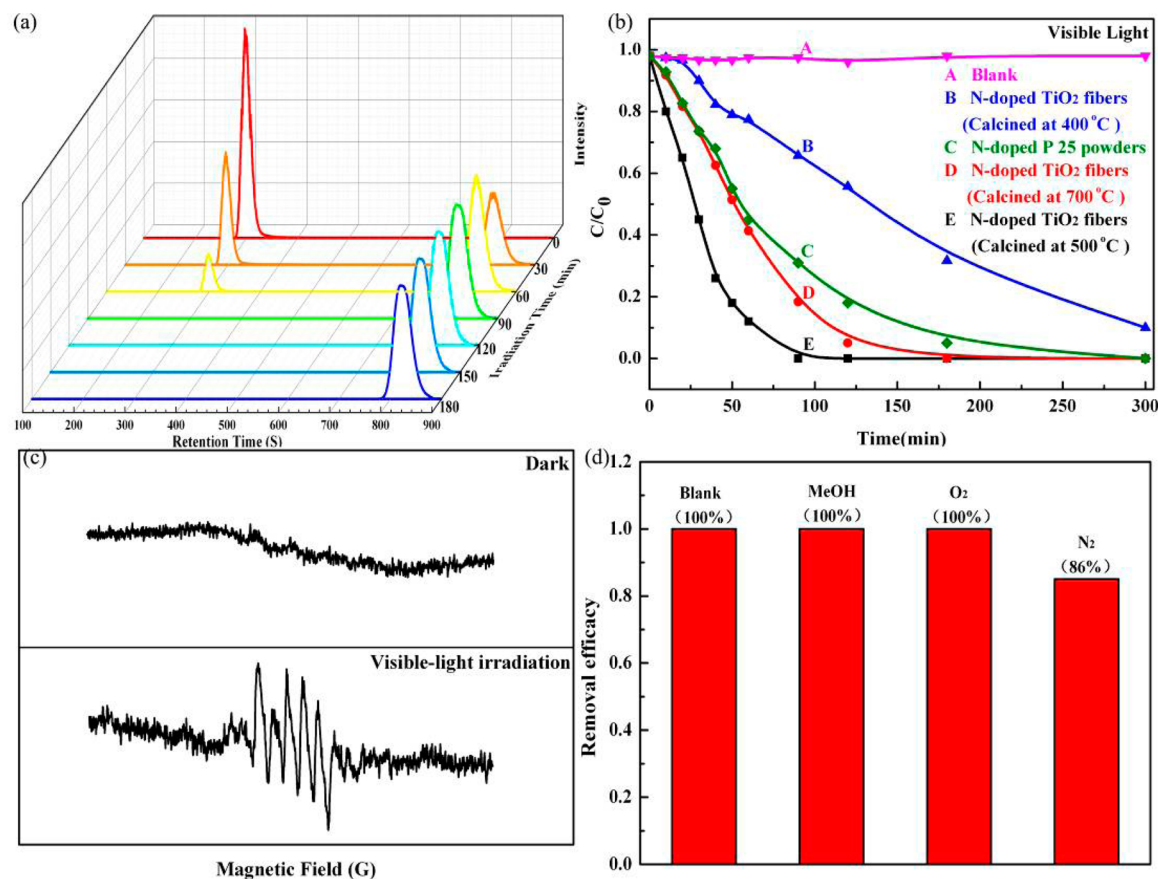

Figure 6. (a) HPLC-MS results of photooxidation of arsenite to arsenate catalyzed by the N-doped TiO$_2$ fibers under visible light irradiation (peak at retention time 300 s refers to As (III); that at 850 s corresponds to As (V)); (b) Photooxidation of As(III) catalyzed by N-doped TiO$_2$ under visible light irradiation; (c) ESR spectra recorded with and without visible light irradiation condition for DMPO-O$_2^{\bullet-}$; (d) Photocatalytic activity of N-doped TiO$_2$ fibers under visible-light irradiation for 90 min in absence and presence of methanol, oxygen, and nitrogen, respectively.
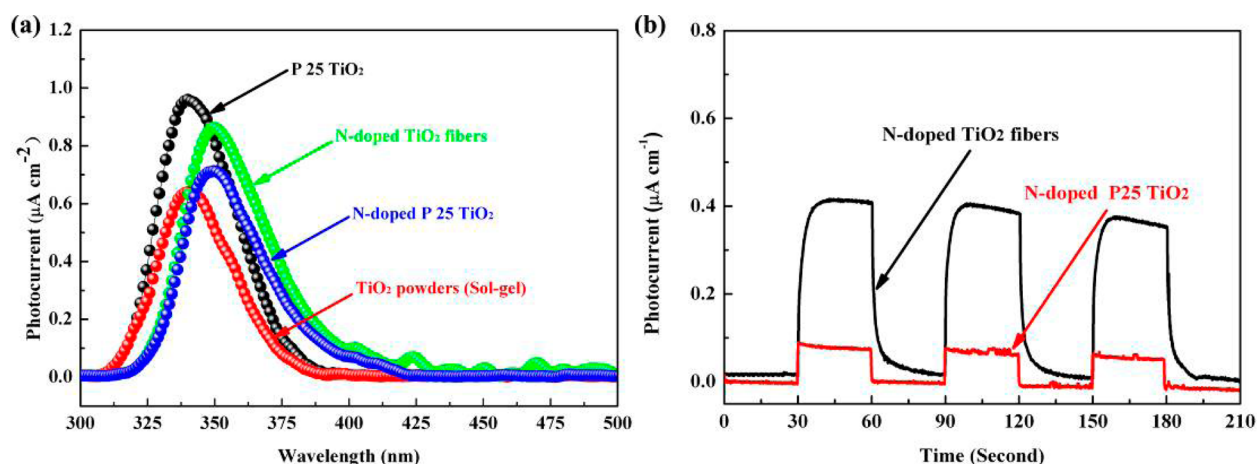
Figure 7. (a) Photocurrent action spectra of P 25 TiO_2, N-doped TiO_2 fibers layer, N-doped P 25 TiO_2 and TiO_2 powders (sol–gel) layer; (b) chronoamperometry of the N-doped TiO_2 fibers and N-doped P 25 TiO_2 layer under visible light irradiation.

DMPO-$O_2^{\bullet-}$ spin adducts could be detected by ESR under visible-light irradiation (Figure 6c). In addition, as shown in Figure 6d, the photocatalysis rate of the system was reduced by saturating the aqueous solution with nitrogen to deplete it of oxygen. In contrast, the effect of $\bullet$OH on the rate of As(III) oxidation could be minimized through the addition of an $\bullet$OH radical scavenger. The results demonstrated that under visible light irradiation, $O_2^{\bullet-}$ was the dominant oxidant in the photocatalytic process. Therefore, the mechanism for oxidation of As(III) catalyzed by N-doped TiO_2 fibers under visible light irradiation could be deduced (Scheme 1).

Scheme 1. Mechanism for the Photooxidation of As(III) Catalyzed by N-Doped TiO_2 Fibers under Visible Light Irradiation
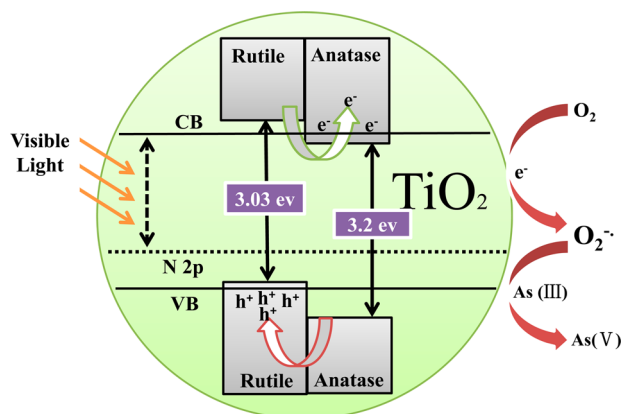
CONCLUSIONS

In summary, we exhibited an alternative approach to prepare N-doped TiO_2 fibers via the electrospinning technique. We speculated that PVP molecules played key roles in promoting the rutile phase to take shape at an unusually low temperature, and ensured the presence of {001} facets at that calcining condition. In addition, the in situ N-doping process did not diminish its UV photoactivity in the As(III) oxidation process. Hence, the proposed electrospinning process has great potential for the production of high-quality TiO_2 to support a broad range of applications.

ASSOCIATED CONTENT

Supporting Information

Nitrogen adsorption/desorption measurements of the TiO_2 fibers; Raman spectra of TiO_2 fibers and TiO_2 powders; XRD patterns of two types of TiO_2 powders; FTIR spectra of the TiO_2 fibers; structure model of the undoped anatase (001)/rutile (101) interface, and decomposition of total DOS of N-doped anatase (001)/rutile (101) interfaces into partial PDOS of the Ti, O, and N orbitals. Photooxidation of arsenic catalyzed by TiO_2 under UV light irradiation. This material is available free of charge via the Internet at http://pubs.acs.org.

AUTHOR INFORMATION

Corresponding Authors
*E-mail: hjliu@rcees.ac.cn. (H.-J.L.)
*E-mail: jhli@mail.tsinghua.edu.cn. (J.-H.L.)

Notes
The authors declare no competing financial interest.

ACKNOWLEDGMENTS

REFERENCES

(1) Yu, J.; Low, J.; Xiao, W.; Zhou, P.; Jaroniec, M. Enhanced Photocatalytic CO_2-Reduction Activity of Anatase TiO_2 by Coexposed {001} and {101} Facets. *J. Am. Chem. Soc.* **2014**, *136*, 8839–42.

(2) Yang, C.; Wang, Z.; Lin, T.; Yin, H.; Lu, X.; Wan, D.; Xu, T.; Zheng, C.; Lin, J.; Huang, F.; Xie, X.; Jiangl, M. Core-Shell Nanostructured "Black" Rutile Titania as Excellent Catalyst for Hydrogen Production Enhanced by Sulfur Doping. *J. Am. Chem. Soc.* **2013**, *135*, 17831–17838.

(3) Feng, X.; Shankar, K.; Varghese, O. K.; Paulose, M.; Latempa, T. J.; Grimes, C. A. Vertically Aligned Single Crystal TiO_2 Nanowire Arrays Grown Directly on Transparent Conducting Oxide Coated Glass: Synthesis Details and Applications. *Nano Lett.* **2008**, *8*, 3781–3786.

(4) Feuz, L.; Jonsson, M. P.; Hook, F. Material-Selective Surface Chemistry for Nanoplasmonic Sensors: Optimizing Sensitivity and Controlling Binding to Local Hot Spots. *Nano Lett.* **2012**, *12*, 873–879.

(5) Bakardjieva, S.; Stengl, V.; Szatmary, L.; Subrt, J.; Lukac, J.; Murafa, N.; Niznansky, D.; Cizek, K.; Jirkovsky, J.; Petrova, N. Transformation of Brookite-type TiO$_2$ Nanocrystals to Rutile: Correlation between Microstructure and Photoactivity. *J. Mater. Chem.* **2006**, *16*, 1709−1716.

(6) Penn, R. L.; Banfield, J. F. Formation of Rutile Nuclei at Anatase {112} Twin Interfaces and the Phase Transformation Mechanism in Nanocrystalline Titania. *Am. Mineral.* **1999**, *84*, 871−876.

(7) Lin, H.; Li, L.; Zhao, M.; Huang, X.; Chen, X.; Li, G.; Yu, R. Synthesis of High -Quality Brookite TiO$_2$ Single-Crystalline Nano-sheets with Specific Facets Exposed: Tuning Catalysts from Inert to Highly Reactive. *J. Am. Chem. Soc.* **2012**, *134*, 8328−8331.

(8) Bickley, R. I.; Gonzalez-Carreno, T.; Lees, J. S.; Palmisano, L.; Tilley, R. J. A Structural Investigation of Titanium Dioxide Photocatalysts. *J. Solid. State. Chem.* **1991**, *92*, 178−190.

(9) Berger, T.; Sterrer, M.; Diwald, O.; Knözinger, E.; Panayotov, D.; Thompson, T.; Yates, J. Light-induced Charge Separation in Anatase TiO$_2$ Particles. *J. Phys. Chem. B* **2005**, *109*, 6061−6068.

(10) Hurum, D. C.; Agrios, A. G.; Gray, K. A.; Rajh, T.; Thurnauer, M. C. Explaining the Enhanced Photocatalytic Activity of Degussa P25 Mixed-phase TiO$_2$ Using EPR. *J. Phys. Chem. B* **2003**, *107*, 4545−4549.

(11) Dai, Y.; Cobley, C. M.; Zeng, J.; Sun, Y.; Xia, Y. Synthesis of Anatase TiO$_2$ Nanocrystals with Exposed {001} Facets. *Nano Lett.* **2009**, *9*, 2455−2459.

(12) Shen, S.; Wang, X.; Chen, T.; Feng, Z.; Li, C. Transfer of Photoinduced Electrons in Anatase-rutile TiO$_2$ Determined by Time Resolved Mid-infrared Spectroscopy. *J. Phys. Chem. C* **2014**, *188*, 12661−12668.

(13) Chen, X.; Mao, S. S. Titanium Dioxide nanomaterials: Synthesis, Properties, Modifications, and Applications. *Chem. Rev.* **2007**, *107*, 2891−2959.

(14) Ide, Y.; Kawamoto, N.; Bando, Y.; Hattori, H.; Sadakane, M.; Sano, T. Ternary Modified TiO$_2$ as a Simple and Efficient Photocatalyst for Green Organic Synthesis. *Chem. Commun.* **2013**, *49*, 3652−3654.

(15) Zhao, Y.; Sun, L.; Xi, M.; Feng, Q.; Jiang, C.; Fong, H. Electrospun TiO$_2$ Nanofelt Surface-Decorated with Ag Nanoparticles as Sensitive and UV-Cleanable Substrate for Surface Enhanced Raman Scattering. *ACS Appl. Mater. Interfaces* **2014**, *6*, 5759−5767.

(16) Chen, X.; Burda, C. The Electronic Origin of the Visible-light Absorption Properties of C-, N- and S- doped TiO$_2$ Nanomaterials. *J. Am. Chem. Soc.* **2008**, *130*, 5018−5019.

(17) Khan, S. U.; Al-Shahry, M.; Ingler, W. B. Efficient Photo-chemical Water Splitting by a Chemically Modified N-TiO$_2$. *Science* **2002**, *297*, 2243−2245.

(18) Mou, Z.; Wu, Y.; Sun, J.; Yang, P.; Du, Y.; Lu, C. TiO$_2$ Nanoparticles- Functionalized N-Doped Graphene with Superior Interfacial Contact and Enhanced Charge Separation for Photo-catalytic Hydrogen Generation. *ACS Appl. Mater. Interfaces* **2014**, *6*, 13798−13806.

(19) Choi, W.; Termin, A.; Hoffmann, M. R. The Role of Metal Ion Dopants in Quantum-sized TiO$_2$: Correlation between Photoreactivity and Charge Carrier Recombination Dynamics. *J. Phys. Chem.* **1994**, *98*, 13669−13679.

(20) Ariga, H.; Taniike, T.; Morikawa, H.; Tada, M.; Min, B. K.; Watanabe, K.; Matsumoto, Y.; Ikeda, S.; Saiki, K.; Iwasawa, Y. Surface-mediated Visible-light Photo-oxidation on Pure TiO$_2$ (001). *J. Am. Chem. Soc.* **2009**, *131*, 14670−14672.

(21) Chen, C.; Li, P.; Wang, G.; Yu, Y.; Duan, F.; Chen, C.; Song, W.; Qin, Y.; Knez, M. Nanoporous Nitrogen-Doped Titanium Dioxide with Excellent Photocatalytic Activity under Visible Light Irradiation Produced by Molecular Layer Deposition. *Angew. Chem., Int. Ed.* **2013**, *52*, 9196−9200.

(22) Nickson, R.; McArthur, J.; Burgess, W.; Ahmed, K. M.; Ravenscroft, P.; Rahmanñ, M. Arsenic Poisoning of Bangladesh Groundwater. *Nature* **1998**, *395*, 338−338.

(23) Pena, M. E.; Korfiatis, G. P.; Patel, M.; Lippincott, L.; Meng, X. Adsorption of As (V) and As (III) by Nanocrystalline Titanium Dioxide. *Water. Res.* **2005**, *39*, 2327−2337.

(24) Xu, Z.; Jing, C.; Li, F.; Meng, X. Mechanisms of Photocatalytical Degradation of Monomethylarsonic and Dimethylarsinic Acids Using Nanocrystalline Titanium Dioxide. *Environ. Sci. Technol.* **2008**, *42*, 2349−2354.

(25) Yu, X.-Y.; Xu, R.-X.; Gao, C.; Luo, T.; Jia, Y.; Liu, J.-H.; Huang, X.-J. Novel 3D Hierarchical Cotton-Candy-Like CuO: Surfactant-Free Solvothermal Synthesis and Application in As(III) Removal. *ACS Appl. Mater. Interfaces* **2012**, *4*, 1954−1962.

(26) Liu, Z.; Zhang, X.; Nishimoto, S.; Murakami, T.; Fujishima, A. Efficient Photocatalytic Degradation of Gaseous Acetaldehyde by Highly Ordered TiO$_2$ Nanotube Arrays. *Environ. Sci. Technol.* **2008**, *42*, 8547−8551.

(27) Ferguson, M. A.; Hering, J. G. TiO$_2$-Photocatalyzed As (III) Oxidation in a Fixed -bed, Flow-through Reactor. *Environ. Sci. Technol.* **2006**, *40*, 4261−4267.

(28) Zheng, J.; Iijima, A.; Furuta, N. Complexation Effect of Antimony Compounds with Citric Acid and its Application to the Apeciation of Antimony (III) and Antimony (V) Using HPLC-ICP-MS. *J. Anal. At. Spectrom.* **2001**, *16*, 812−818.

(29) Perdew, J. P.; Burke, K.; Ernzerhof, M. Generalized Gradient Approximation Made Simple. *Phys. Rev. Lett.* **1996**, *77*, 3865−3868.

(30) Dudarev, S. L.; Botton, G. A.; Savrasov, S. Y.; Humphreys, C. J.; Sutton, A. P. Electron-energy-loss Spectra and the Structural Stability of Nickel Oxide: An LSDA+U study. *Phys. Rev. B* **1998**, *57*, 1505−1509.

(31) Kresse, G.; Joubert, D. From Ultrasoft Pseudopotentials to the Projector Augmented-wave Method. *Phys. Rev. B* **1999**, *59*, 1758−1775.

(32) Kresse, G.; Furthmuller, J. Efficient Iterative Schemes for Ab Initio Total-energy Calculations Using a Plane-wave Basis Set. *Phys. Rev. B* **1996**, *54*, 11169−11186.

(33) Zhang, J.; Li, M.; Feng, Z.; Chen, J.; Li, C. UV Raman Spectroscopic Study on TiO$_2$. I. Phase Transformation at the Surface and in the Bulk. *J. Phys. Chem. B* **2006**, *110*, 927−935.

(34) Zhou, Y.; Fichthorn, K. A. Microscopic View of Nucleation in the Anatase-to -Rutile Transformation. *J. Phys. Chem. C* **2012**, *116*, 8314−8321.

(35) Romero, L.; Binions, R. On the Influence of DC Electric Fields on the Aerosol Assisted Chemical Vapor Deposition Growth of Photoactive Titanium Dioxide Thin Films. *Langmuir* **2013**, *29*, 13542−13550.

(36) Wu, B.; Guo, C.; Zheng, N.; Xie, Z.; Stucky, G. D. Nonaqueous Production of Nanostructured Anatase with High-energy Facets. *J. Am. Chem. Soc.* **2008**, *130*, 17563−17567.

(37) Liao, Y.; Zhang, H.; Que, W.; Zhong, P.; Bai, F.; Zhong, Z.; Wen, Q.; Chen, W. Activating the Single-Crystal TiO$_2$ Nanoparticle Film with Exposed {001} Facets. *ACS Appl. Mater. Interfaces* **2013**, *5*, 6463−6466.

(38) Serpone, N. Is the Band Gap of Pristine TiO$_2$ Narrowed by Anion- and Cation- doping of Titanium Dioxide in Second-generation Photocatalysts? *J. Phys. Chem. B* **2006**, *110*, 24287−24293.

(39) Kuznetsov, V. N.; Serpone, N. On the Origin of the Spectral Bands in the Visible Absorption Spectra of Visible-Light-Active TiO$_2$ Specimens Analysis and Assignments. *J. Phys. Chem. C* **2009**, *113*, 15110−15123.

(40) Wang, J.; Tafen, D. N.; Lewis, J. P.; Hong, Z.; Manivannan, A.; Zhi, M.; Li, M.; Wu, N. Origin of Photocatalytic Activity of Nitrogen-Doped TiO$_2$ Nanobelts. *J. Am. Chem. Soc.* **2009**, *131*, 12290−12297.

(41) Zhu, K.; Vinzant, T. B.; Neale, N. R.; Frank, A. J. Removing Structural Disorder from Oriented TiO$_2$ Nanotube Arrays: Reducing the Dimensionality of Transport and Recombination in Dye-sensitized Solar Cells. *Nano Lett.* **2007**, *7*, 3739−3746.